Quantum Effect Devices

- *Millimeter-wave, Teraherz and Infrared Devices*

- *Terahertz Lasers Based on Intersubband Transitions*

- *AlGaAs/GaAs HBT with Enhanced Forward Diffusion*

- *An On-chip Frequency-domain Submillimeter-wave Spectrometer*

- *Superconducting Persistent Current Qubits*

- *Integrated Superconducting Device Technology for Qubit Control*

- *Resonant Cancellation of Off-resonant Transitions in a Multilevel Qubit*

- *Relaxation of a Coherent Quantum System During Premeasurement Entanglement*

- *Inductance Effects in the Persistent Current Qubit*

- *Engineering Josephson Oscillators*

- *Vortex Ratchets*

- *Discrete Breathers in Josephson Arrays*

Millimeter-wave, Teraherz and Infrared Devices

Personnel

E. Atmaca, H. Callebaut, E. Duerr, K. Konistis, J. Montoya, B. Williams (Q. Hu)

Sponsorship

Millimeter-wave and THz frequencies (f = 0.1-10 THz) remain one of the most underdeveloped frequency ranges, even though the potential applications in remote sensing, spectroscopy, and communications are great. This is because the millimeter-wave and THz frequency range falls between two other frequency ranges in which conventional semiconductor devices are usually operated. One is the microwave frequency range, and the other is the near-infrared and optical frequency range. Semiconductor devices which utilize the classical diffusive transport of electrons, such as diodes and transistors, have a high frequency limit. This limit is set by the transient time and parasitic RC time constants. Currently, electron mobility and the smallest feature size which can be fabricated by lithography limit the frequency range to below several hundred GHz. Semiconductor devices based on quantum mechanical interband transitions, however, are limited to frequencies higher than those corresponding to the semiconductor energy gap, which is higher than 10 THz for most bulk semiconductors. Therefore, a large gap exists from 100 GHz to 10 THz in which very few devices are available.

Semiconductor quantum-effect devices (which can be loosely termed "artificial atoms"), including both vertically grown quantum-well structures and laterally confined mesoscopic devices, are human-made quantum mechanical systems in which the energy levels can be chosen by changing the sizes of the devices. Typically, the frequency corresponding to the intersubband transitions is in the millimeter-wave range ($\Delta E \sim 1\text{-}4$ meV) for the lateral quantum-effective devices, and THz to infrared for the vertical quantum wells. It is therefore appealing to develop ultrahigh-frequency devices, such as THz lasers utilizing the intersubband transitions in these devices.

In our group, we are systematically investigating physical and engineering issues that are relevant to devices operating from millimeter-wave to THz frequencies. Specifically, we are working on THz lasers based on intersubband transitions in quantum wells, ultrahigh-frequency heterostructure bipolar transistors based on phonon-enhanced forward diffusion, and on-chip terahertz spectrometers using ultrafast photoconductive switches.

Terahertz Lasers Based on Intersubband Transitions

Personnel
B. Williams, H. Callebaut, E. Atmaca, and Q. Hu, in collaboration with Prof. M. Melloch at Purdue University, and J. Reno at Sandia National Lab

Sponsorship
NSF, ARO, NASA, AFOSR

Unipolar intersubband-transition lasers (also called quantum-cascade lasers) at mid-infrared wavelengths were developed only recently at Bell Laboratories. This achievement is remarkable, but the technique used in the original quantum-cascade lasers will not be directly applicable for the longer-wavelength THz range because of two major obstacles. First, the energy levels corresponding to THz frequencies (1 THz = 4 meV) are quite narrow, so the requirements for the design and fabrication of suitable quantum wells are demanding. Because of the narrow separation between subband levels, heating and electron-electron scattering will have a much greater effect. Also, the small energy scales of THz photons make the detection and analysis of spontaneous emission (a crucial step toward developing lasers) quite difficult.

Second, mode confinement, which is essential for any laser oscillation, is difficult at longer wavelengths. Conventional dielectric-waveguide confinement is not applicable because the evanescent field penetration, which is proportional to the wavelength and is on the order of several tens of microns, is much greater than the active gain medium of several microns. Currently, we are investigating to overcome these two obstacles in order to develop intersubband-transition lasers. We have made good progress in generating and detecting THz emission signals and on developing a novel mode confinement method using metallic waveguide structures.

One of our MQW structures for THz emission is shown in Figure 1, in which the conduction band profile and the square of the wave functions were calculated self-consistently from Schrödinger and Poisson equations. The device is formed by a triple-well structure using GaAs/$Al_{0.3}Ga_{0.7}As$ materials, as shown in the dashed box. This structure is essentially a three-level system (marked as E_3, E_2, and E_1 in Fig. 1), which is required for any lasers. Because there is no recombination

involved in unipolar intersubband lasers, electrons can be "reused" many times. Consequently, many identical triple-well modules can be cascade-connected, and the emission power and the mode confinement factor can be increased substantially. Due to translational symmetry, design analysis needs to focus only on one module, provided there are no global space charges and high-field domains.

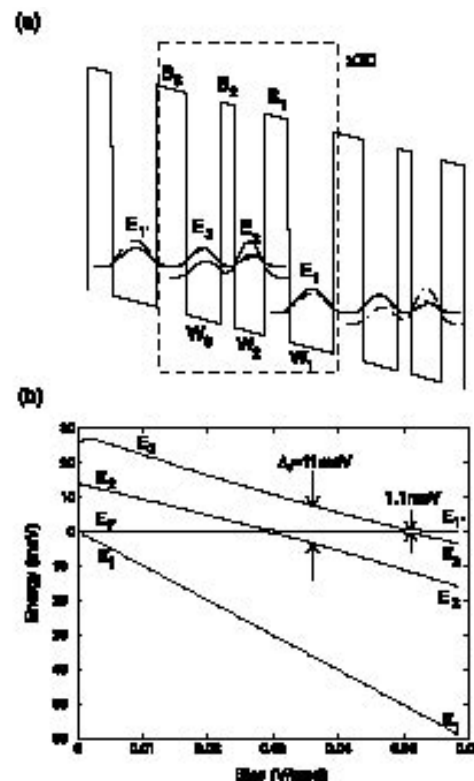In order to measure the intersubband THz emission and resolve its spectra, we constructed a set-up that

Fig. 1: Schematic of a three-level system based on a triple quantum-well structure. The radiation transition takes place between E_3 and E_2, and the fast LO-phonon emission keeps the level E_2 empty.

included a Fourier transform infrared spectrometer (FTIR) with a composite Si bolometer as its detector. The system's schematic is shown in Fig. 2. We have improved this system and perfected our measurement techniques so that THz emission measurements can be routinely performed on our emitters with output power levels of 1-10 pW.
The MQW structures were grown using molecular-beam epitaxy (MBE). The emission spectra reveal a clear peak due to the E3-E2 intersubband emission. A
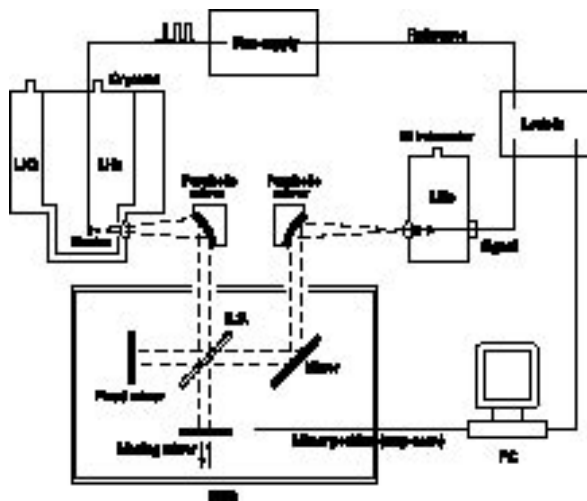
representative spectrum taken at 5 K is shown in Figure 3 (Top). Spectra were also taken with the cold stage cooled with liquid nitrogen to 80 K. A measured spectrum is shown in Figure 3 (Bottom).

Recently, we have designed and fabricated a new THz emission structure based on vertical (or intrawell) radiative transition, in which the radiative transition takes
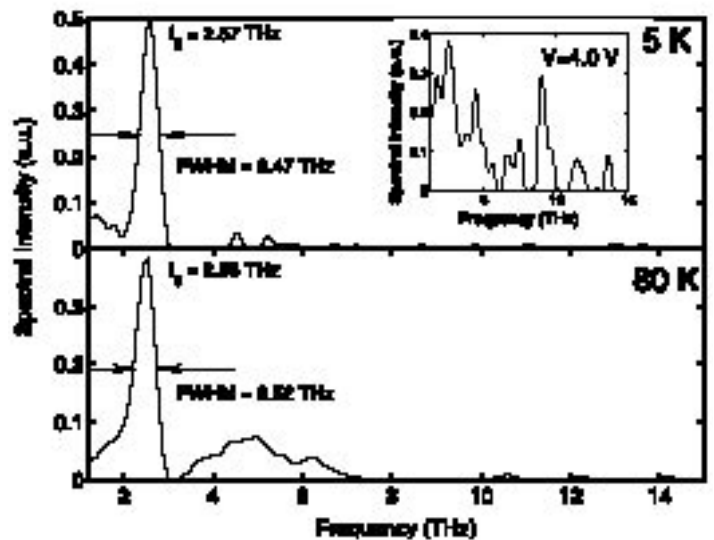

Fig. 2: Far-infrared measurement set-up that uses a Fourier transform spectrometer to spectrally resolve the emitted THz signals.

Fig. 3: Spectrally resolved THz intesubband emission take at (Top)5~K and (bottom) 80-~K under a bias of 1.6~V. The inset shows the spectrum under a 4.0~V bias.

place between two subbands primarily located in one quantum well. The profile of the quantum-well structure is shown in Figure 4. In this scheme, because of the strong spatial overlap of the two subband wavefunctions, the radiative transition has a large dipole moment and is less sensitive to interface roughness scattering. As a result, the radiation efficiency is higher and the emission linewidth is narrower than that of interwell transition scheme shown earlier. However, the pumping and depopulation now rely on electron-electron scattering, instead of the electron-phonon scattering as in the previous case. The analysis of electron-electron scattering is a complicated manybody problem. It becomes manageable only recently with a numerical simulation package developed by Prof. P. Harrison at University of Leeds. The structure shown in Fig. 4 was designed with the aid of this numerical code. According to our design analysis, the electron-electron scattering among the closely spaced subbands should be much faster than

that between the two radiative subbands, which will yield a population inversion between the two.

Our preliminary emission measurement showed very encouraging results, as shown in Figure 5. The linewidth of the spontaneous emission is only half of that in the previous case, as expected from the intrawell scheme. Furthermore, since the fast LO-phonon scattering is not utilized in this scheme, the relaxation rate and consequently the current density is lower than those of the previous structures, yielding a much lower dc power dissipation. At this stage, we do not yet know which structure will offer the best opportunity to achieve a high degree of population inversion, and we plan to full explore both structures for the development of THz lasers.
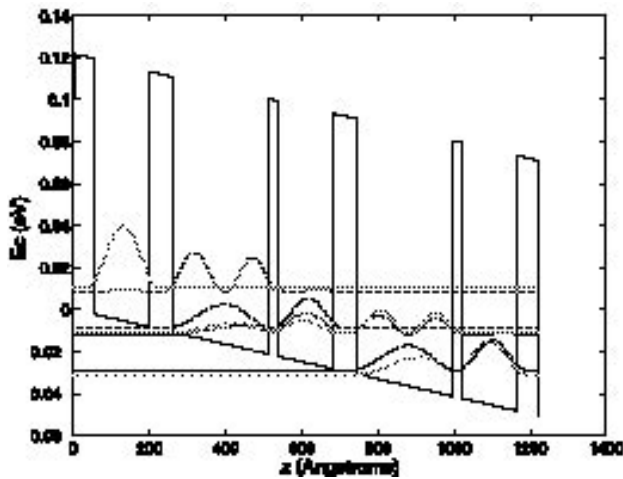

Fig. 4: Scheme of an intrawell radiative transition structure. The radiative dipole moment should be large and the emission linewidth should be narrow, due to the strong spatial overlap of the two wavefunctions. Population inversion can be facilitated by electron-electron scattering.
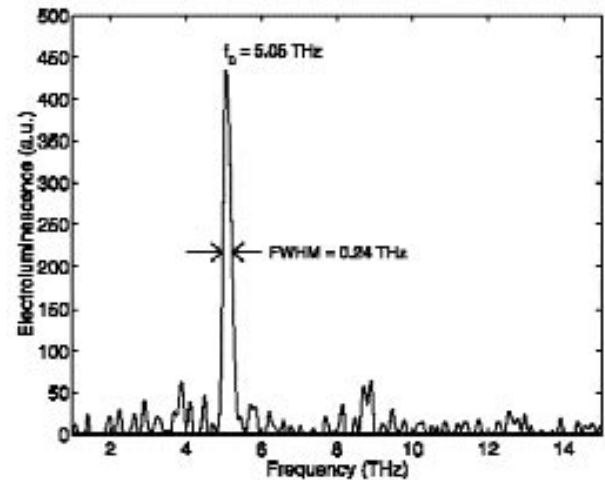

Fig. 5: Spectrum of spontaneous emission taken at the designed bias voltage. The center frequency is close to the designed value and the linewidth is as narrow as 1 meV (0.24 THz).

AlGaAs/GaAs HBT with Enhanced Forward Diffusion

Personnel

K. Konistis and Q. Hu, in collaboration with J. Reno at Sandia National Lab

One of the key limits of high-frequency operation of bipolar transistors is the base transient time, which is proportional to the square of the base width when the base transport is dominated by diffusion. Consequently, high-frequency bipolar transistors tend to use thin bases (<100 nm) that results in a short base transient time and a high cut-off frequency f_T. However, for high frequency operations, it is not the current gain that matters most. Rather, it is the unilateral power gain that determines the operating frequency of any three-terminal devices. The frequency f_{max}, at which the power gain is unity, is determined by both f_T and RC time constant. Because of the peculiar geometry of bipolar transistors, the electrical contact to the base is always made from the side. Thus, a thin base, which is important to yield a high f_T, will inevitably result in a high sheet resistance and a lowering of fmax. It is this difficult trade-off between f_T and f_{max} that lead Prof. S. Luryi and his co-workers to propose a novel heterostructure bipolar transistor, whose band diagram is shown in Figure 6.

The main feature of this novel HBT is that its base is graded like a staircase. The height of each step Δ is slightly greater than the LO-phonon energy in GaAs (36 meV). Thus, electrons will encounter very fast LO-phonon emission scattering (with a time ~0.1 ps) when they go over the edge of a step. Consequently, backward diffusion is prohibited. In a way, the edge of each step resembles and performs a similar function as the base-collector interface: any injected excess minority carrier will be quickly swept down the energy potential. As a result, each step acts like a minibase, as far as the diffusion transport is concerned. The resulting minority carrier concentration assumes a nearly periodic distribution provided that the energy drop is greater than the sum of LO-phonon and thermal energy to ensure a fast scattering and prohibit backward diffusion. The total base transient time is therefore approximately N times the transient time of each step, whose width can be as narrow as 30 nm, yielding a high f_T. On the other hand, all the N steps are connected in parallel for the base contact, reducing the base resistance by an approximate factor of N. The combination of a thin effective base and small base resistance will yield a high f_{max}.

The use of LO-phonon scattering as a resetting mechanism introduces the concept of independent cascade of base transport factors. In our analysis, the intrinsic part is modeled by device physics whereas the extrinsic are treated as lumped circuit elements. A simple approach that captures most of the physics is to define the transport as the product of the individual base steps assuming perfect resetting LO mechanism. As a result, the total base transport factor is a simple product of the transport factor of each step, as shown in Figure 7. It can be seen clearly, as the number of steps N increases, the amplitude of the base transport factor increases, resulting in a higher cut-off frequency.

One interesting result of our analysis is the existence of resonances of the unilateral power gain. Their physical mechanism is closely linked with the current-phase delay. A base structure introduces both phase delay and magnitude attenuation of current. As the frequency of operation increases, the phase delay increases and at a certain frequency the voltage and current acquire opposite phases, which will yield a resonance if the amplitude attenuation is not too overwhelming. A short base offers small phase delay and resonance occurs at high frequencies where the magnitude attenuation is strong. On the other hand, a long base may provide a large phase delay but the heavy attenuation at low frequencies smoothes out the unilateral gain peaks. For a multi-step base, the total phase delay is the sum of each step, while the total attenuation is the product of each step, enhancing the possibilities of achieving resonance. As can be seen in Figure 7, the base transport factor of multi-step base HBTs crosses the real axis with an appreciable amplitude, Figure 8 shows both the

current gain and unilateral power gain as a function of frequency for N =1-6. Clearly, even though f_T decreases somewhat as the number of steps N increases, f_{max} barely changes due to the reduced base resistance of high-N bases. Furthermore, resonance can be achieved above 100 GHz by using multi-step base HBTs, which is promising for the development of high-frequency fundamental oscillators.
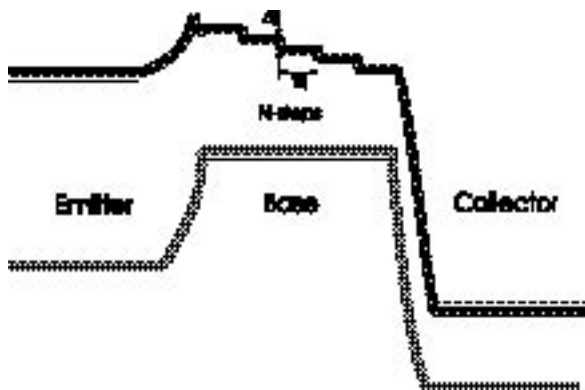

Fig. 6: Energy band diagram of an HBT with stepwise base. The energy drop Δ at each step is slightly greater than the LO-phonon energy (36 meV) in GaAs. Thus, electrons encounter very fast LO-phonon emission scattering (with a time ~0.1 ps) when they go over the edge of a step. Consequently, backward diffusion is prohibited and forward diffusion is enhanced.
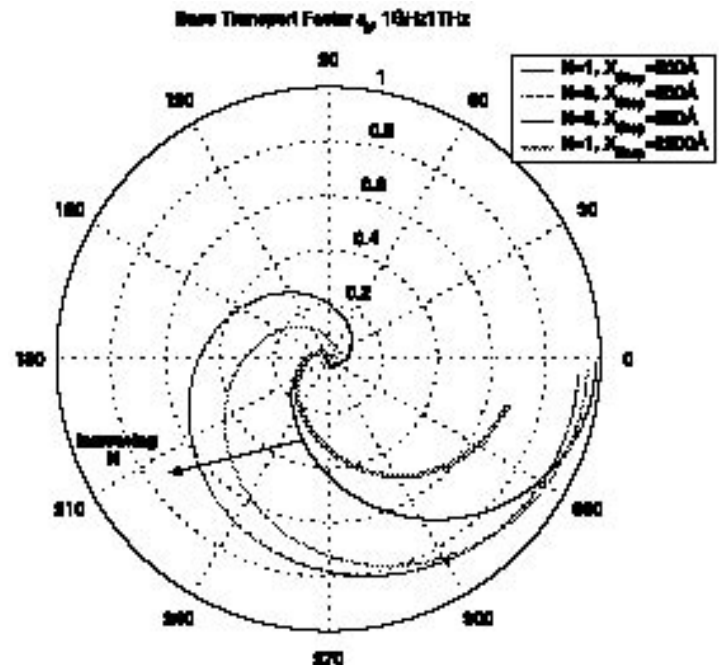

Fig. 7: Polar plot of base transport factor in frequency, for N steps and XStep step size.

An On-chip Frequency-domain Submillimeter-wave Spectrometer

Personnel
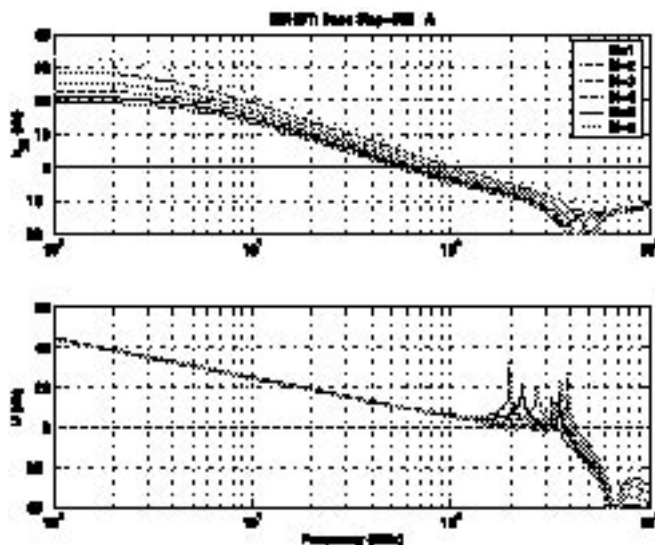J. Montoya and Q. Hu

Sponsorship
Rosenblith Fellowship

Fig. 8: Current gain h21 and Unilateral power gain U in frequency for XStep =500 Å and variable number of steps. The resonance (peaks in U) is clearly shown above 100 GHz, which is promising for the development of high-frequency fundamental oscillators.

Because of the frequency limitation of semiconductor electronic devices, measurement instruments such as network analyzers can operate only below approximately 100 GHz. Thus, even if ultrahigh-frequency HBTs can be developed, they can only be directly measured up to 100 GHz, with higher-frequency performance extrapolated according to certain frequency roll-off models. Clearly, such an extrapolated measurement will not be applicable to measuring high-frequency resonance. It will be very useful to develop on-chip systems that can characterize device performance up to THz frequencies. A promising component for such systems is ultrafast photoconductive switches made of low-temperature-grown (LTG) GaAs materials. When pumped with two coherent laser beams, such switches can generate and detect photocurrent with a modulation frequency beyond one THz.

Furthermore, photoconductive emitters and receivers are attractive as components of sub-millimeter-wave spectroscopy systems because of their tunability, compactness and ability to be monolithically integrated with antennas, transmission lines and microelectronic devices. Such systems can be classified either as time-domain or frequency-domain systems. Time-domain systems, which contain a photoconductive pulse emitter and sampler excited by a mode-locked laser, are the most investigated. They have been used for free-space characterization of semiconductor materials, and on-chip characterization of ultrafast devices and circuits with 2.7 ps time resolution. The frequency resolution is the inverse of the time span over which the propagating pulse is sampled. This span is determined by the length of an optical delay line, which usually results in a frequency resolution broader than 1 GHz.

The emitter and receiver of a frequency-domain spectrometer will be pumped by two coherent cw laser beams with frequencies ω_1 and ω_2, instead of short

laser pulses. If the response time is sufficiently fast, the emitter switch will generate an ac photocurrent with a frequency $|\omega_2-\omega_1|$, which can easily exceed 1 THz. Illuminated by the same two laser beams with a controlled delay, the receiver switch can be used to perform a homodyne detection of the ac photocurrent generated from the emitter. In combination with high-frequency transmission lines, they can form on-chip spectrometers with THz bandwidths. Fig. 9 illustrates a schematic of such a spectrometer that can be used to characterize common-emitter performance of high-frequency HBTs.

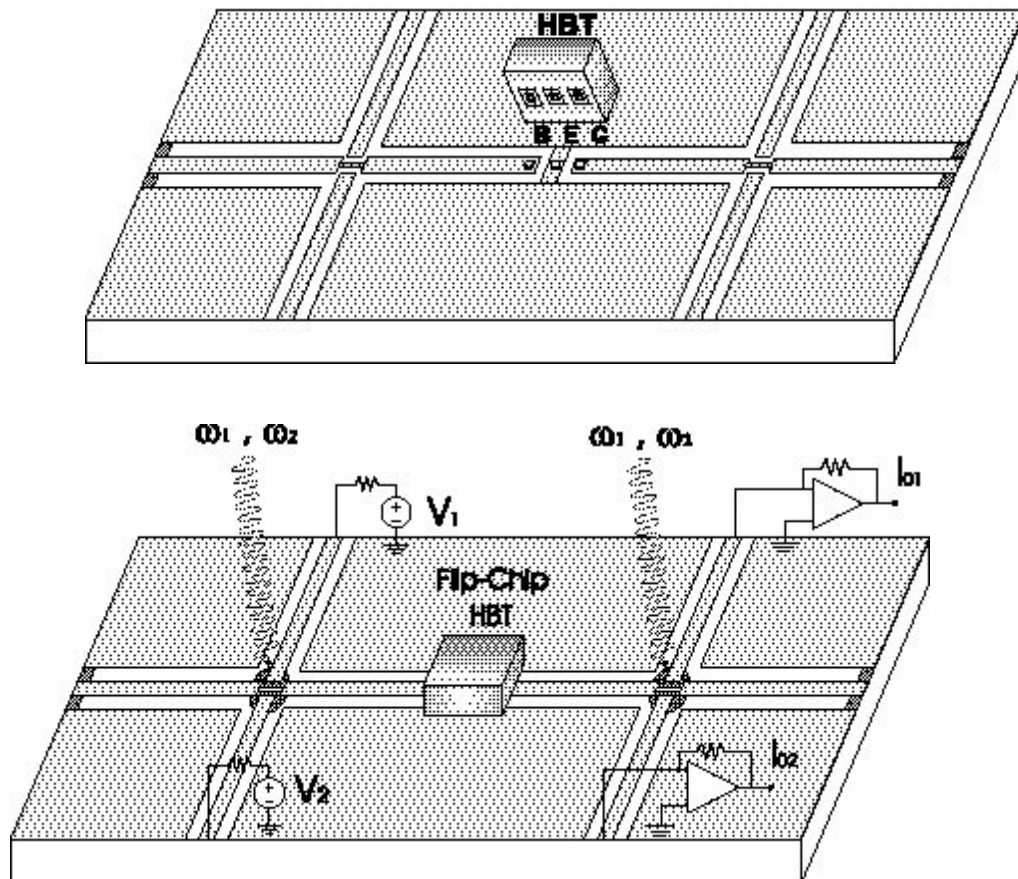Because of the broad bandwidth (>1 THz) and a high frequency resolution (better than 1 MHz), such a

Fig. 9: Schematic of a on-chip spectrometer that uses ultrafast photoconductive switches to generate and detect ultrahigh-frequency signals.

spectrometer is also adequate for molecular line spectroscopy. In combination with microchambers, the spectrometer can be part of a microfluidic, "lab on a chip"-type circuit, which can be used as on-chip sensors for chemical and biological agents. As the first step in the development of an on-chip frequency-domain spectrometer, we have investigated the performance of an on-chip transceiver containing only uninterrupted coplanar waveguides (CPWs).

Our circuit, shown in Figure 10a, has a biased pump photoconductor and an unbiased probe photoconductor connected by a main CPW, and other parasitic CPWs which provide DC electrical contact to the photoconductors. We excited propagating electromagnetic waves at the pump by illuminating the pump photoconductor with two overlapping diode laser beams with a difference frequency $f = \omega_2 - \omega_1$. We performed homodyne detection of those waves by illuminating the probe with a delayed portion of the same laser beams. The relative delay between the pump and probe beams is the phase Φ. The output DC current I_{o1} should vary sinusoidally with Φ, $I_{o1}(\Phi) = I_o\cos(\Phi+\delta)$, because of the homodyne detection performed at the probe photoconductor. The argument of cosine contains two terms: the phase Φ, which is due only to the path lengths of the pump and probe beams; and the phase δ, which describes the response of the circuit and any device or specimen inserted in it. For example, δ may be non-zero because of the dispersion of the CPWs or circuit resonance. Our aim was to measure I_o and δ as functions of f. Together, I_o and δ contain all the information necessary for coherent spectroscopy.
We fit the measured spectra to a model based on the circuit shown in Figure 10b. The two active regions of the pump photoconductor are modeled as current sources. Similarly, the single utilized active region of the probe
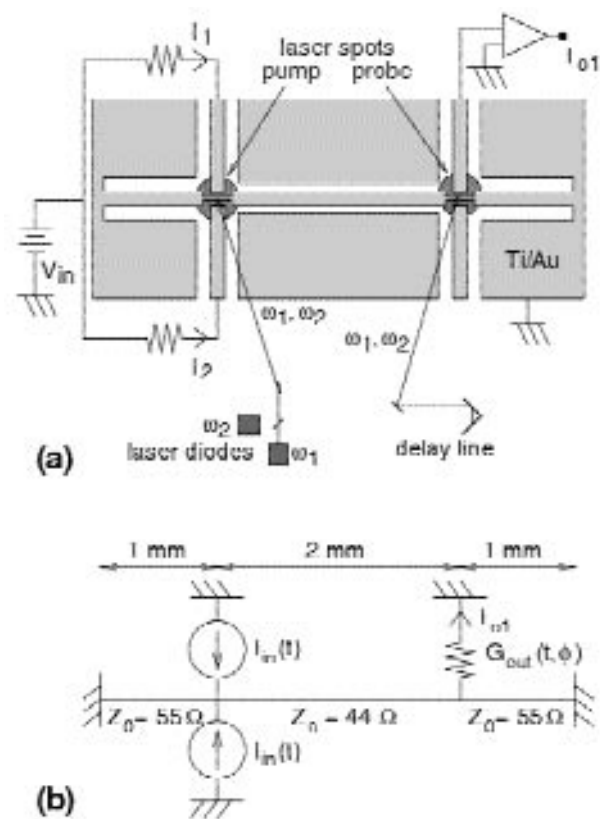

Fig. 10: (a) Diagram of the experimental circuit, showing its electrical bias and optical input. (b) Microwave circuit model of the experimental circuit.

photoconductor is modeled as the time-varying conductance. We assume that the CPWs have a propagation constant $\Gamma = \alpha(f) + j_2 \pi f / v_p$, where $\alpha(f)$ is the attenuation constant to be fit to the data, and v_p is the phase velocity of a coplanar transmission line on a semi-infinite GaAs substrate. We use standard microwave circuit analysis to calculate I_{o1}, the Φ-dependent DC current generated at the probe.

Our model was fit to the data with reasonable fitting parameters. The agreement between the model and the measured results is quite good, validating the microwave-circuit analysis of our on-chip submillimeter-wave transceiver.
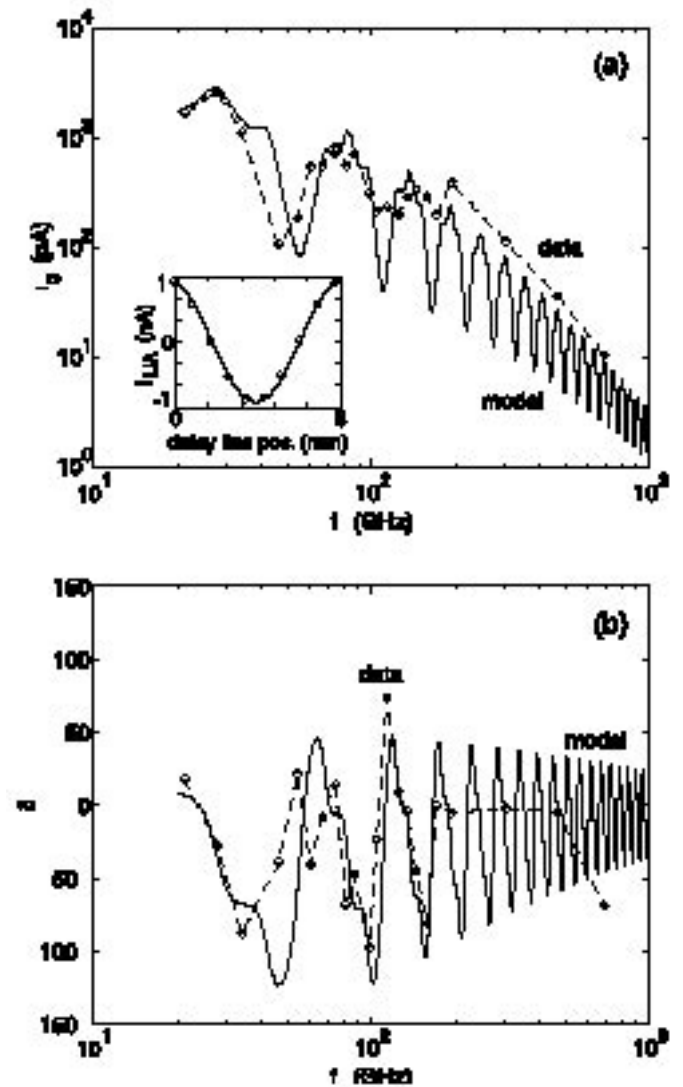

Fig. 11: Measured data and model of the amplitude and phase spectra (a) $I_0(f)$ and (b) $\delta(f)$. Inset: Output of lock-in amplifier vs. delay line position at f=27.9 GHz, compared to a best-fit sinusoid.

Superconducting Persistent Current Qubits

Personnel

L. Tian, D.S. Crankshaw, D. Nakada, and C.H. van der Wal[1] (L. Levitov, S. Lloyd, J.E. Mooij, C.J. Harmans, A.C.J. ter Haar[1], F.K. Wilhelm[1], R.N. Schouten, and T.P. Orlando)

Quantum computers are devices that store information on quantum variables such as spin, photons, and atoms, and process that information by making those variables interact in a way that preserves quantum coherence. Typically, these variables consist of two-state quantum systems called quantum bits or 'qubits'. To perform a quantum computation, one must be able to prepare qubits in a desired initial state, coherently manipulate superpositions of a qubit's two states, couple qubits together, measure their state, and keep them relatively free from interactions that induce noise and decoherence.

We have designed a superconducting qubit that has circulating currents of opposite sign as its two states. The circuit consists of three nano-scale aluminum Josephson junctions connected in a superconducting loop and controlled by magnetic fields.

Figure 12a shows a SEM image of the persistent current qubit (inner loop) and the measuring dc SQUID (outer) loop. The Josephson junctions appear as small "breaks" in the image.
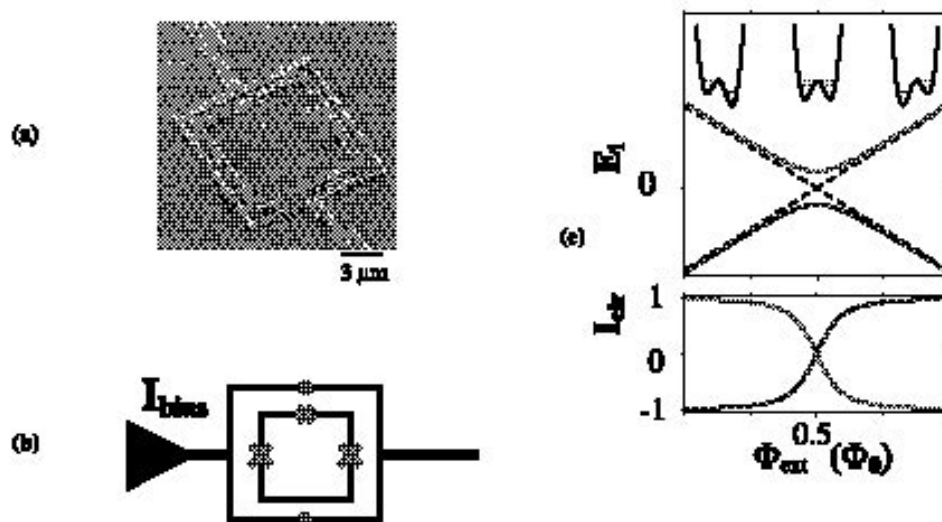

Fig. 12: (a) SEM image of the persistent current qubit (inner loop) surrounded by the measuring dc SQUID. (b) a schematic of the qubit and measuring SQUID, the x's mark the Josephson junctions. (c) The energy levels for the ground state (dark line) and the first excited state of the qubit versus applied flux. The double well potentials are shown schematically above. The lower graph shows the circulating current in the qubit for both states as a function of applied flux. The units of flux are given in terms of the flux quantum.

A schematic of the qubit and the measuring circuit is shown in Figure 12b, where the Josephson junctions are denoted by x's. The qubit loop is 5x5 μm^2 with aluminum-oxide tunnel junctions, microfabricated at the TU Delft, by a shadow evaporation technique. (This is in contrast to the samples fabricated at MIT's Lincoln Laboratory that are made in niobium by photolithographic techniques on a trilayer of niobium-aluminum oxide-niobium wafer.) The capacitance of the junction is estimated to be about 3 fF and the ratio of the Josephson energy to the charging energy is about 40. The inductances of the inner qubit loop and the outer measuring loop are about 11 and 16 pH respectively, with a 7 pH mutual inductive coupling.

The energy levels of the ground state (dark line) and the first excited state (light line) are shown in Figure 12c near the applied magnetic field of 0.5 Φ_0 in the qubit loop. Classically the Josephson energy of the two states would be degenerate at this bias magnetic field and increase and decrease linearly from this bias field, as shown by the dotted line. Since the slope of the *E* versus magnetic field is the circulating current, we see that these two classical states have opposite circulating currents. However, quantum mechanically, the charging energy couples these two states and results in a energy level repulsion at $\Phi_{ext} = 0.5 \Phi_0$, so that there the system is in a linear superposition of the currents flowing in opposite directions. As the applied field is changed from below $\Phi_{ext} = 0.5 \Phi_0$ to above, we see that the circulating current goes from negative, to zero at $\Phi_{ext} = 0.5 \Phi_0$, to positive as shown in the lower graph of Figure 1c. This flux can be measured by the sensitive flux meter provided by the dc SQUID.
Figure 13a shows the circulating current as inferred from the dc SQUID measurements for various applied microwave frequencies. The curves are offset for clarity, and each curve shows the expected change from negative circulating current at low applied flux, to zero at half a flux quantum, and then to positive current at higher flux. This clearly shows that the qubit has the change in flux profile expected of the ground state. When microwaves are applied at the energy difference matching the difference between the ground state and the first excited state, then a transition is induced from the ground state to the first excited state. These are shown by the resonant-like structures in each curve. A plot of the distance in Φ_{ext} at the resonance from $\Phi_{ext} = 0.5 \Phi_0$ is shown in the figure on the left. Quantum mechanically the energy is expected to follow the form

$$\Delta E = \sqrt{\left[2 I_p \left(\Phi_{ext} - 0.5 \Phi_0\right)\right] + \left(2 V\right)^2}$$

where I$_p$ is the circulating current and V is the tunneling matrix element between the two circulating current states at $\Phi_{ext} = 0.5 \Phi_0$. The inset shows a fit to the curve which gives an energy gap of about 600 MHz and a circulating current of about 500 nA as expected. These results are among the first experimental verification of the superposition of macroscopic circulating current states.

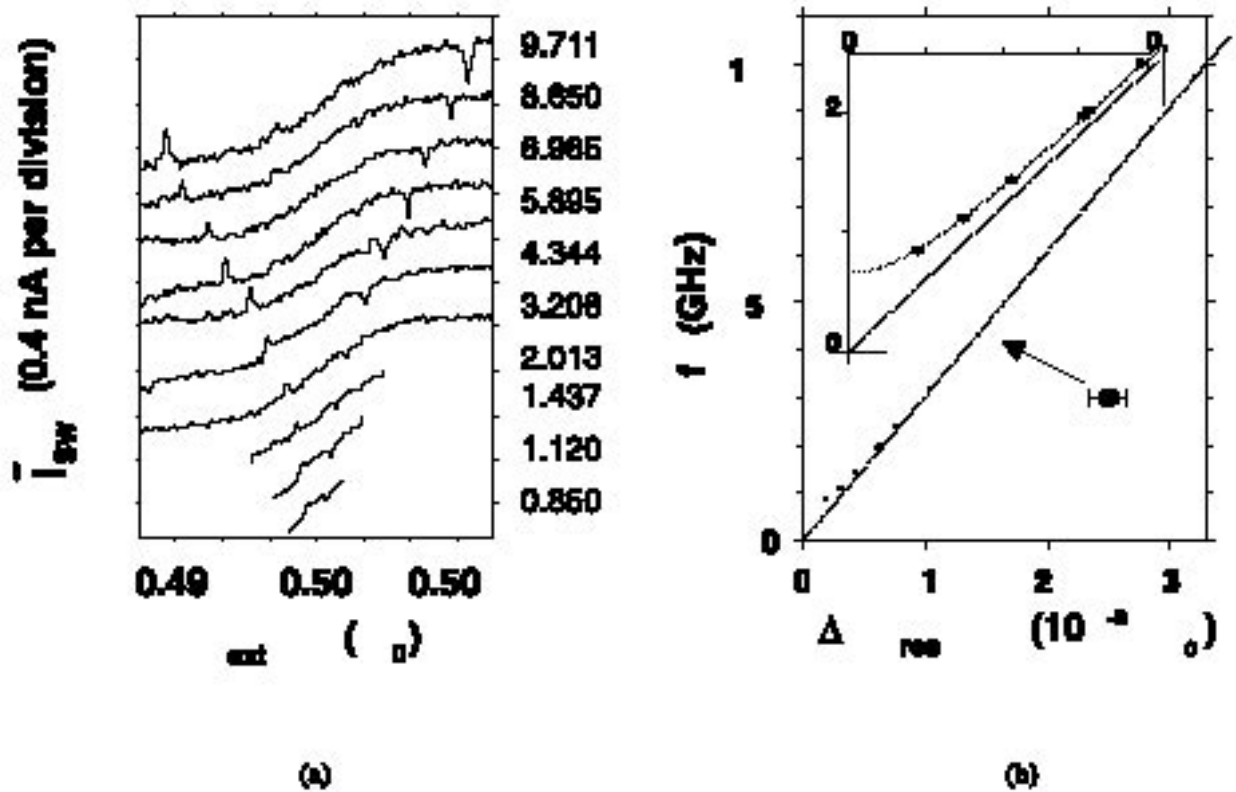*(1) Delft U. of Technology, The Netherlands*

Continued

Fig. 13: (a) The circulating current as inferred from the dc SQUID measurements for various applied microwave frequencies. The curves are off-set for clarity. (b) Half the distance in Φ_{ext} measured between the resonant peaks and the dips at different frequencies f. The inset shows the low frequency data points. The grey line is a linear fit through the high frequency points and zero. The black line is a fit of the quantum theory.

Integrated Superconducting Device Technology for Qubit Control

Personnel

D. Nakada, M. O'Hara, K. Berggren1, T. Weir1, E. Macedo1, and R. Slattery1 (T. P. Orlando)

Quantum computing requires the time-dependent control and readout of qubit couplings. Critical to the project of quantum computing is therefore the integration of quantum devices with conventional superconducting digital and analog electronics that will be used to provide classical circuitry for control and readout functions of the quantum computer. The "classical" and "quantum" devices can be integrated using inductive coupling between chips bonded by a flip-chip process. There exists a classical electronics family based on superconductive electronics – Single Flux Quantum (SFQ) logic – having the capability of operating well above 100 GHz clock speeds. Such devices can be used to execute many control operations before substantial decoherence occurs in the persistent current qubit – a feature that could benefit other solid-state qubit technologies with long coherence times. The flip-chip process is not limited to the field of quantum computing but has applications in any technology that would benefit from SFQ electronics.

We have designed experiments to couple current magnetically from a carrier chip, onto a flipped chip, and back onto a different area of the carrier chip where the resulting magnetic field was sensed with a dc SQUID.

The flipped chip lies less than 2 μm above the carrier chip with less than 2 μm of linear misalignment. The magnetic coupling between the current line and dc SQUID was enhanced due to the presence of a transformer loop on the flipped chip. To show this, we compared the effective mutual inductance between the control current and the dc SQUID with and without the presence of the flipped chip. For quantum computing implementation, the flipped chip would carry the qubits while the carrier chip will contain the control and readout circuitry for determining the state of the qubit.

Our next step will be to design SFQ circuitry for manipulation and control of the superposition states of the persistent current qubit. Using an on-chip oscillator, we propose using timed microwave pulses to excite the qubit from the ground state to the first excited state. We also plan to increase coupling between the carrier chip and flip-chip by improving alignment as well as decreasing the chip-to-chip distance. We hope our efforts demonstrating the control of a single qubit will be an initial step towards a full-scale quantum computer.
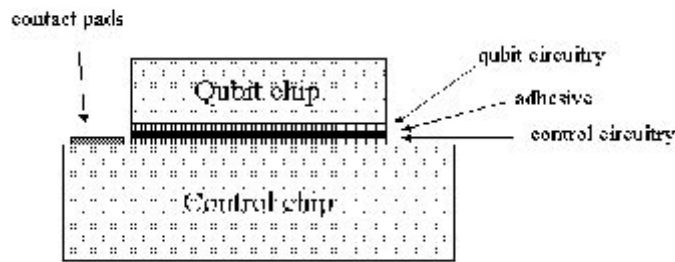
(1) MIT Lincoln Lab

Fig. 14: Cross section of a packaged chip. For our initial experiment, the "qubit" chip contained the transformer loop while the "control chip" included the control line and DC SQUID, coupled together via the transformer loop

Resonant Cancellation of Off-resonant Transitions in a Multilevel Qubit

Personnel
L. Tian, S. Lloyd, J. E. Mooij[1], F. K. Wilhelm[1] (T. P. Orlando)

Off-resonant effects are a significant source of error in quantum computation. Physical qubits are not ideal two level systems, but have many higher levels that are irrelevant for qubit operation. The off-resonant transitions to the higher levels of a qubit during gate operations are a particularly important form of intrinsic qubit error. Numerical simulation shows that this effect can introduce an error as high as 1% in the superconducting persistent current qubit, which is significantly higher than the noise from environmental fluctuations of qubit.

To correct this error and accomplish quantum computation, we study the effect of these higher levels on qubit dynamics during qubit operation by a group theoretical approach. We prove that the errors can be completely avoided by applying a time varying Hamiltonian. The transformations on an N-level quantum system are described by the N^2 dimensional compact Lie group $U(N)$. By applying controllable pulses of Hamiltonian H_I, with $[H_0, H_2] \neq 0$, any transformation in $U(N)$ can be reached within N^2 number of pulses. This shows that the transformation on a given quantum system can be restricted to the lowest two levels with time dependent pumping.

This study was then generalized to the qubit error resulting from qubit interaction. Qubit interaction is necessary for the CNOT gate which is needed for the universal set of quantum logic gates. But qubit interaction also introduces operational errors by additional transition matrix elements during gate operations. By mapping the interacting qubits as a multilevel quantum system with higher levels, the same method can be applied to correct the errors in the coupled qubit system.
By extending the idea of dynamic pulse control by Viola and Lloyd, we designed a pulse sequence that cancels the leakage to the higher levels to arbitrary accuracy with $O(N)$ number of pulses, N being the number of higher levels. This approach exploits `bang-bang' control techniques where the dynamics of the qubit and its environment is manipulated by fast pulses that flip the qubit state. The influence of the environment being averaged out, the qubit evolves in the error-free subspace. This method relies on the ability to apply the pulses rapidly compared with the correlation time of the environment. This is an open loop control method.

In the proposed method, we apply resonant pulses between different eigen-states to cancel the unwanted off-resonant transitions to the higher levels. All the pulses applied have the same time duration. By adjusting the amplitudes and phases of the pulses, the leakage to higher levels can be completely suppressed at the end of operation. Since all the pulses in this sequence have the same pulse length, they can be combined into one pulse with slightly different parameters. This method for protecting quantum information is complementary to quantum error correcting codes and the `bang-bang' technique mentioned above. Like the bang-bang method, it has the advantage that it does not require extra qubits to enact. The proposed method protects against a different class of errors from those corrected by the methods of Viola, however. Dynamic pulse control can be used in conjunction with quantum error correcting codes and bang-bang decoupling methods.

(1) Delft University of Technology, The Netherlands

Recent experiments on superconducting loops have demonstrated macroscopic quantum effects. These

Relaxation of a Coherent Quantum System During Premeasurement Entanglement

Personnel

L. Tian, S. Lloyd, J.E. Mooij[1], F.K. Wilhelm[1], C.H. van der Wal[1], and L. Levitov (T.P. Orlando)

experiments used a dc SQUID to measure the magnetic flux generated by the persistent currents of the macroscopic quantum states. Due to the inductive interaction between the qubit and the SQUID, the relaxation and dephasing of the qubit are limited by the entanglement with the measurement device as well as its coupling to the solid-state environment. We studied the effect of the meter (SQUID) environmental spectrum density on the qubit dynamics within the spin-boson formalism. The results can be applied to optimizing the measurement circuit to get the best measurement efficiency.

As the ramping current increases, the interaction between the qubit and the dc SQUID entangles the qubit and the SQUID. This entanglement brings indirect interaction between the qubit and the SQUID environment and introduces additional noise to the qubit. As this interaction does not commute with the qubit Hamiltonian, it influences the qubit dynamics non-trivially. The effective spectrum density seen by the qubit is renormalized due to the presence of the meter degrees of freedom and has a different shape from the spectrum density seen by the meter.

The qubit dynamics can be described within the master equation approach when the interaction with the environment is weak. From this approach the relaxation and decoherence of the qubit, also called the transversal relaxation and the longitudinal relaxation rates, are determined by the spectrum density of the environment. As the inductive interaction induces a σ_ζ interaction between the qubit and SQUID environment, the qubit Hamiltonian H_0 has non-commuting σ_x component with the sz interaction, a transversal interaction that flips the qubit and eventually relaxes the it in the qubit eigen basis is created. This transversal interaction depends quadratically on both the tunneling between the two localized qubit states and the inductance coupling.

Our study also suggests that by engineering the measurement circuit, we can optimize the spectrum density seen by the qubit and minimize the relaxation of the qubit due to various environmental fluctuations. Within the theoretical framework, arbitrary designs can be analyzed and compared.

(1) Delft University of Technology, The Netherlands

Inductance Effects in the Persistent Current Qubit

Personnel

D. S. Crankshaw (T. P. Orlando)

In the original description of the persistent current qubit, the inductance was neglected in the energy level calculations. The effects of the small inductance in the PC qubit can be included by using a perturbative approach. This technique simplifies the numerical calculations by reducing the dimensionality of the Schrödinger equation that must be solved. Consider a circuit with b branches, each with a Josephson junction, connected at n nodes to form m meshes (loops). In general, the dimensionality of the Schrödinger equation for such a circuit is $b=n+m-1$. If the inductance of each mesh is small so that $\beta_L<<1$, the energy levels can be calculated by ignoring the inductances (i.e., setting $\beta_L=0$). The dimensionality of the resulting Schrödinger equation is the number of independent nodes $n-1 < b$. Moreover, we find that the Hamiltonian can be written in the form

$$H_b = H_n(\Theta_n) + H_M(I_M) + \Delta H(\langle \Theta_n \rangle,\langle I_M \rangle)$$

The full Hamiltonian, H_b, of b variables is written in terms of three Hamiltonians: the first, $H_n(\Theta_n)$, is of the form of what one would write with $\beta_L=0$, and has $n-1$ node variables Θ_n. $H_n(\Theta_n)$ is periodic in each of these variables. The second, $H_m(I_m)$, is of the form of a simple harmonic oscillator of the m mesh (circulating) current variables. The last term is a correction term that can often be neglected in calculating the energy levels. If we can separate the Hamiltonian this way, the mesh Hamiltonian and the correction term are easily solved analytically (since one is a simple harmonic oscillator and the other is calculated from the expectation values of the other Hamiltonians' variables), leaving only the node Hamiltonian, which has a lower dimensionality than the branch Hamiltonian and is periodic in all its variables. This is solved numerically. (This reduces the computational time of $O(N^b)$ for H_b to $O(N^{n-1})$, $O(m)$, and $O(nN+m)$ for the terms H_n, H_m, and ΔH respectively, where N is the number of discretized elements of the quantum phase variables.)

When the qubit is modeled in a way to facilitate this derivation (see Figure 15), it reduces to the simplified equation

The first term is the original, zero inductance solution to the qubit energy, the second term is the harmonic

$$E=E_q(f)+(n+\tfrac{1}{2})\hbar\omega_0 -$$

$$\tfrac{1}{2}L_m I_c^2\left(\frac{\alpha}{1+2\alpha}\right)^2\left(\langle\sin(2\tilde{\Theta}_m+2\pi f)\rangle-\langle 2\cos\Theta_p \sin\tilde{\Theta}_m\rangle\right)^2 .$$
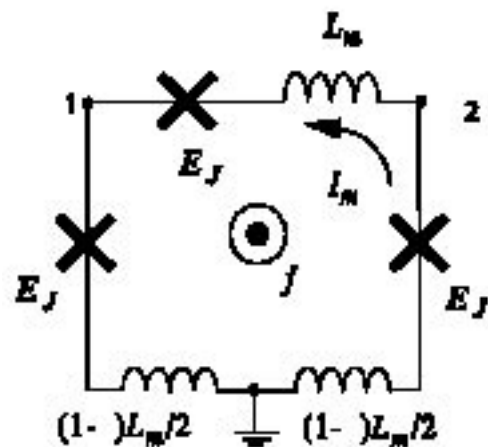

Fig. 15: The circuit used to derive the PC qubit Hamiltonian with inductance.

Engineering Josephson Oscillators

Personnel
D.S. Crankshaw, E. Trías (T.P. Orlando)

oscillator of the circulating current variables, and the final term is the correction term. The result for a realistic value of the qubit inductance is shown in Figure 16, which indicates that the deviation from the zero inductance solution in negligible.
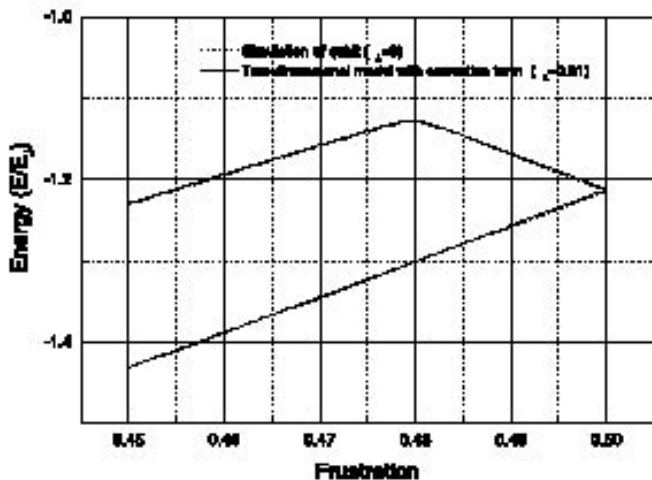

Fig. 16: A comparison of PC qubit with and without a small inductance. The β_L was chosen to reflect the estimated geometric inductance of the fabricated qubit. The region shown in the diagram is that used for quantum computation.

As the telecommunications revolution pushes for denser utilization of the spectrum, there is a need to develop inexpensive sources and detectors that operate in the 100 GHz to several THz range. It is precisely in this range that Josephson junctions provide an almost ideal solid state, current controllable source.

Arrays of junctions provide for relatively large power but due to non-linearities they can exhibit diverse complex spatiotemporal patterns. Experiments, simulations, and analysis were performed on a broad range of discrete arrays of Josephson-junction oscillators in order to understand their ability to produce coherent radiation. Networks ranging from single square and triangular plaquettes to one- and two-dimensional arrays were studied. In each array, the junctions are identical, and the arrays are driven by dc bias currents. Although few analytical results are known for these systems, we study the technically interesting solutions which can be represented as traveling waves. It is in this mode that the devices can be used as submillimeter wave sources.

Using the mathematical technique of harmonic balance it is possible to create an equivalent linear circuit of a Josephson network that is operating in a traveling wave mode. Though the non-linearity of the system allows for mixing of all the harmonics, in underdamped systems we find that the first harmonic is orders of magnitude stronger than the rest. In general, any variable can be decomposed in terms of its dc and ac spectrum. If we further restrict the ac component to a single frequency as suggested by our simulations, then the branch current and voltage across a junction can be written as:

$$I = I_{DC} + i_{ac}e^{j\omega t}$$

$$V = V_{DC} + v_{ac}e^{j\omega t}$$

$$I_c = e^{j\kappa},$$

$$I_M = \frac{v_{ac}}{j\omega} \frac{e^{-j\kappa}}{2}.$$

Our equivalent circuit then consists of a dc bias circuit and a mixing circuit that creates the first harmonic. Figure 17 depicts the equivalent circuit. Here k represents the phase difference between the first harmonic and the rotating part of the Josephson oscillation, and the mixing current, I_M, represents the nonlinear interaction between them. This equivalent circuit makes it possible to use powerful circuit theoretic tools to understand a Josephson network.

This model has been used to design a matched load detector. A Josephson junction can be used to detect and measure power, and designing a detector to match the impedance of an array allows us to measure the power produced by the array. Experiments measuring the powe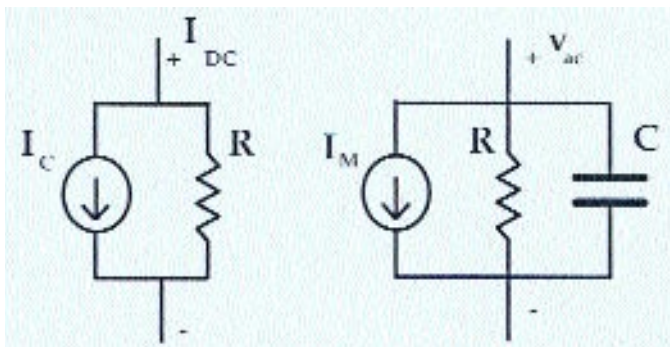r which an array of 54 overdamped junctions delivers to an impedance match load attest to the usefulness of our model, giving a strong qualitative correlation between the predicted and measured power for varying magnetic flux (measured in units of frustration, the number of flux quantum per unit cell).

Currently, much of our oscillator work is designed to drive quantum circuits, such as the qubit and the quantum ratchet. The oscillators designed for this work are less focused on maximum power than minimum decoherence, meaning that designs may benefit from deliberately unmatched impedances. The exacting requirements of this application further test the accuracy of our model in a challenging regime.

Fig. 17: Equivalent circuit for a Josephson junction in a voltage state and with a single harmonic. Non- linearity is captured by I_M which is a mixing current that describes the interaction between the rotating Josephson phase and its first harmonic.
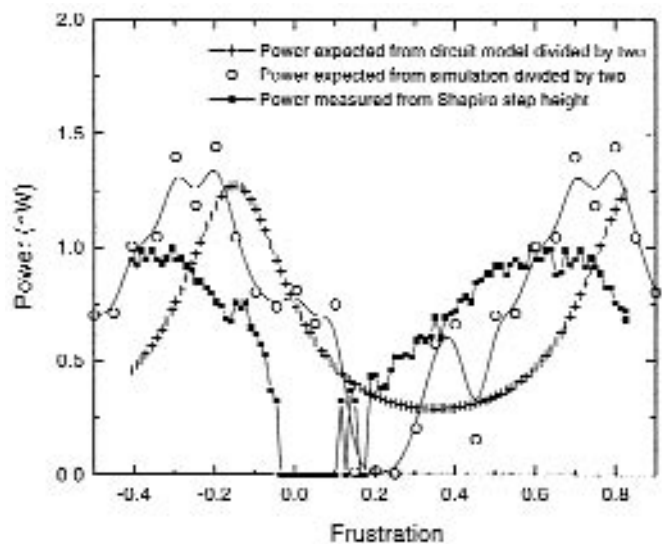

Fig. 18: The power produced by the array, experimental measurements compared to nonlinear simulation and linear circuit model predictions. The array is biased at $V_{arr} = 0.1035$ mV.

Vortex Ratchets

Personnel

K. Segall, E. Trías, J. J. Mazo (T.P. Orlando)

Disorder and noise are not always undesirable in physical systems. An interesting, almost counterintuitive result is obtained when one studies the transport of a Brownian particle in an asymetric potential. Under certain circumstances these systems can display net particle transport, despite the absence of any gradients. Originally proposed by Feynman, these systems with a so-called "ratchet" potential display a unique variety of behavior and suggest several possible applications. Ratchets were initially proposed as a model for molecular motors in biological organisms, and more recently as a model system in studying dissipative and stochastic processes in nanoscale devices. Ratchets have also been proposed as voltage and current rectifiers in cryogenic circuits, as devices for phase separation, and for a method of flux cleaning in superconducting thin films. A ratchet mechanism has also been proposed as a method to prevent mound formation in epitaxial film growth.

A ratchet potential is a periodic potential which lacks reflection symmetry (in 1D $V(x)$ not equal to $V(-x)$, see Figure 19. A consequence of this symmetry breaking is the possibility of rectifying non-thermal or time correlated fluctuations. This can be understood intuitively. In Figure 19, it takes a smaller dc driving force to move a particle from a well to the right than to the left. In other words, the spatial symmetry of the dc force is broken. When driven out of equilibrium, such as under an ac drive or time-correlated noise, particles show net directional motion in the smallest slope direction. This effect can be studied theoretically and used in devices in which selection of particle motion is desired.

In Josephson-junction parallel arrays, kinks (or vortices) behave as particles in which this idea of Brownian rectification can apply. The applied current is the driving force. The potential is determined by the size and geometry of the junctions in the array. If the potential has the form of a ratchet potential, then the current needed to move the kink in one direction is different than the current to move it in the opposite direction.

We have designed, fabricated and measured circular parallel arrays (rings) in order to study the motion of kinks through a ratchet potential. Figure 20 shows typical IV's for the different measured rings. Figure 20 (a) is for a regular ring with a single trapped vortex. The IV is symmetric with respect to applied current direction. As the current is increased from zero the voltage remains at zero, which implies that the vortex is pinned. As the current increases beyond the depinning value, a voltage is developed, implying that the kink is now moving around the ring.- At higher currents voltage steps develop, which are resonances between the moving vortex and the electromagnetic modes of the ring. Figure 20 (b) is a ring where the junctions have alternating critical currents. We again see that the IV is symmetric with respect to current direction and that there are voltage steps. Figure 20-(c) is a ring with alternating areas. The characteristics are similar to that of ring 20 (b). Since for these three rings the depinning current is the same in the positive and negative direction, we can infer that the kink is traveling in a symmetric pinning potential. This was expected from our models.

Figure 20 (d) shows an IV for the ring with both alternating critical currents and areas. The IV of this ring is qualitatively different from the other rings. We see that the depinning current in the positive direction is ~65% of the depinning current in the negative direction. Such a difference implies that the kink is traveling in a ratchet potential. We also note that there are different voltage steps excited in the up and down direction.

We have measured the depinning of trapped kinks in this ratchet potential and compared it with the other circular arrays. We find experimentally and numerically that the depinning current depends on the direction of the applied current only in the ratchet ring. We also

find other properties of the depinning current versus applied field, such as a long period and a lack of reflection symmetry, which we can explain analytically. In future experiments we plan to drive the system out of equilibrium with an ac current, and look for the directed transport of the kinks. Such experiments will begin

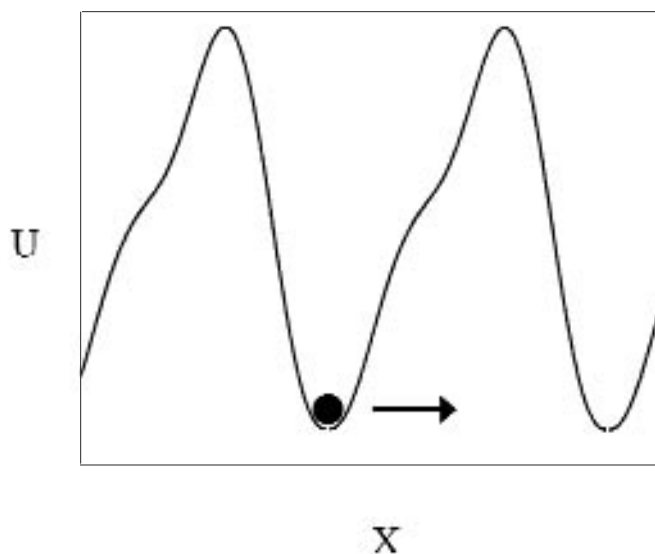to verify the essential predictions of ratchet behavior.

Fig. 19: Example of a ratchet potential. The particle sitting on the well requires less force to move through the first peak to the right than to move to the left. Therefore, there is a preferred direction of motion.
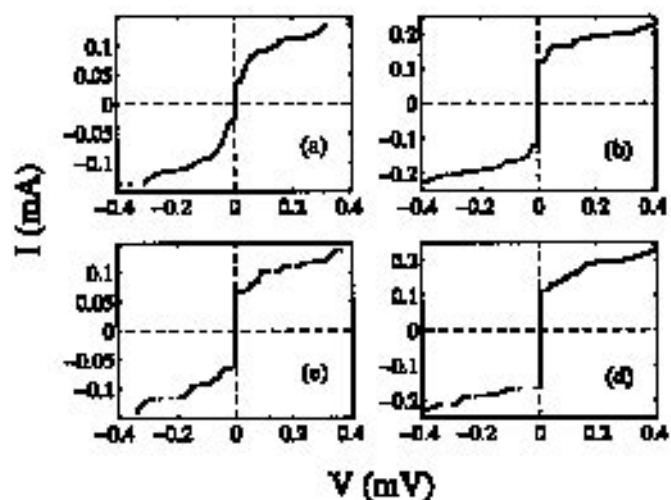

Fig. 20: Sample IV curves for the four measured rings. Rings (a), (b), and (c) have symmetric IV's as the current is swept in the positive and negative direction. Ring (d) is the ratchet ring as can be seen from the difference in the depinning current in the positive and negative direction.

Discrete Breathers in Josephson Arrays

Personnel

K. Segall, J.J. Mazo, E. Trías, A. Brinkman (T. P. Orlando)

Linear models of crystals have been instrumental in developing a physical understanding of the solid state. Many thermodynamic properties, transport properties, and photon interaction properties of a crystal can be understood by modeling it as an atomic lattice with fixed harmonic interactions. Certain properties of solids, however, cannot be understood in this model. In describing thermal expansion, for example, one often finds that the elastic constants of the atomic interactions depend on temperature or the volume so as to make their interaction non-linear. The usual approach in treating these so-called anharmonic effects is to use a generalized Taylor expansion for the lattice interaction that includes more than just the harmonic term.

Until quite recently anharmonic effects were studied as perturbations to the fully solvable harmonic model, which uses extended plane waves as its basis. Then it was discovered that the non-linearity may lead to *localized* vibrations in the lattice that are not adequately described by a plane wave approach. These intrinsically localized modes have been termed discrete breathers because their amplitudes oscillate around a few sites in the lattice and do not depend on impurities for their localization. Discrete breathers have been shown to be generic modes in many non-linear lattices, hence they have been the object of great theoretical and numerical attention. However, until recent work by our group (and one other) they had yet to be detected in any experiment.

We have designed experiments to detect localized modes (discrete breathers) in Josephson-junction anisotropic ladder arrays biased by dc external currents. We have done numerical simulations of the dynamics of such ladders at experimentally accessible values of the parameters of the array. We have also developed a method for exciting a breather in the array and detected their existence experimentally. We distinguish between two families of solutions which present different voltage patterns in the array. Both types are robust to random fluctuations and exist over a range of parameters values and array sizes.

Our anisotropic ladders contain junctions of two different critical currents: I_{ch} for the horizontal junctions and I_{cv} for the vertical ones. The anisotropy parameter h can then be defined as $h=I_{ch}/I_{cv}$. The horizontal junctions act as the coupling term between the vertical junctions. The dependence of a junction's current is sinusoidal with the phase; hence the interactions of the vertical junctions are anharmonic, with h serving as the measure of interaction strength. Figure 21 shows schematically two simple localized modes. The arrows indicate junctions that are rotating. All the other junctions librate at their equilibrium points. Type A breathers (Figure 22 (a)), are characterized by one vertical and two horizontal rotating junctions; type B breathers (Figure 22 (b)), are characterized by one vertical and four horizontal rotating junctions.

Since a rotating junction outputs a dc voltage, the breather solutions can easily be detected by measuring the average voltage of the different vertical and horizontal junctions. Figure 22 shows a typical result. We prepare the system in an initial condition with a breather located in the middle junction of the array (number 5) at $I_a = 1.4$ mA. We then decrease the applied current slowly. We start with the signature measurement of the breather: junction five is rotating at V_g while the neighboring junctions, V_4 and V_6, are at zero voltage. The horizontal junctions, V_{4T} and V_{5T}, have the expected value of $V_g/2$. As the current is decreased the breather persists until 0.8 mA, at which point the single-site breather destablizes, creating a two-site breather. We are currently investigating the properties of single-site and multi-site breathers in these Josephson lattices.

In addition to studying the discrete breathers them-

selves, we can also study how they interact with non-localized excitations such as vortices. We have fabricated arrays with paramaters that should allow for the simultaneous existence of a breather and a vortex. We have simulated numerically their interaction and find that the breather acts as a pinning center for the vortex motion. The pinned vortices become trapped in a potential well with an activation energy of about 22 Kelvin. We are currently working to verify these predictions experimentally.

Just as the discovery of soliton solutions led to the deeper understanding of non-linear systems and to subsequent applications outside the solid state community, it is hoped that the study and measurement of discrete breathers will add a new tool with which to further unlock mysteries of complex non-linear systems.
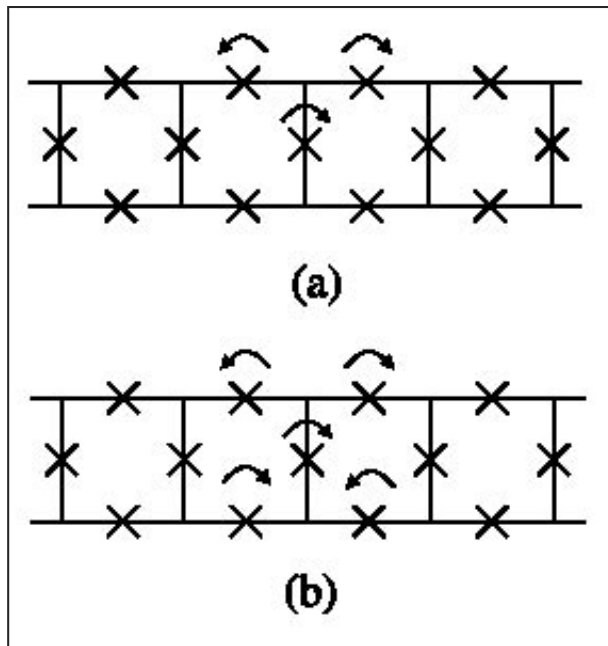

Fig. 21: Schematic picture of breather solutions in ladder array: type A (a) and type B (b) breathers. Arrows are associated with rotating junctions.
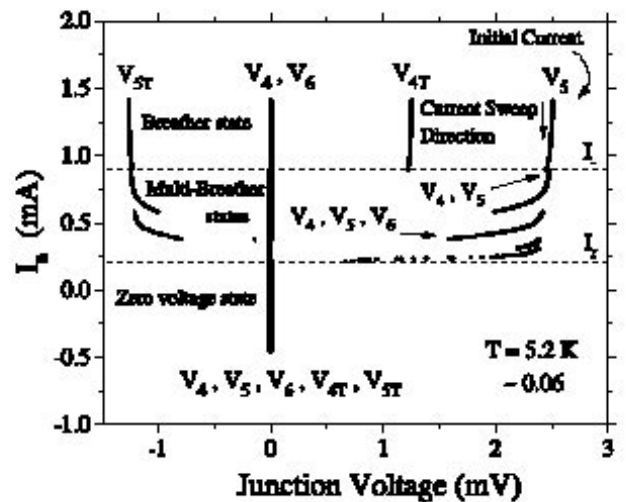

Fig. 22: Measured time-averaged voltages of five junctions in the center of an array as the applied current is decreased. We have biased the ladder at 1.4 mA and excited a breather. Then the applied current is decreased.